Journal of Advanced Ceramics
先进陶瓷
ISSN 2226-4108
CN 10-1154/TQ
清华大学出版社 Tsinghua University Press
SciOpen

J Adv Ceram 2026, **15**: 9221359

https://doi.org/10.26599/JAC.2026.9221359

Research Article

Decoupling the factors governing diffuse phase transition and relaxor–ferroelectric evolution in high-entropy tetragonal tungsten bronze ceramics

Chongyang Zhang[1], Weijia Guo[1,2,*], Xingchen Zhang[1], Bowen Yin[1], Yutian Lu[1], Hui Zhang[1], Zhenxing Yue[1,*]

[1] *State Key Laboratory of New Ceramic Materials, School of Materials Science and Engineering, Tsinghua University, Beijing 100084, China*

[2] *State Key Laboratory of New Ceramic Materials, Beijing Tsinghua Institute for Frontier Interdisciplinary Innovation, Beijing 102202, China*

* Corresponding author.

E-mail: W. Guo, guoweijia0315@163.com;

Z. Yue, yuezhx@mail.tsinghua.edu.cn

Received: June 2, 2026; Revised: August 11, 2026; Accepted: August 12, 2026

Abstract: High-entropy engineering has emerged as an effective strategy for tailoring structural disorder and functional responses in tetragonal tungsten bronze (TTB) ferroelectrics. However, how configurational entropy, crystal structure, modulation characteristics, and relaxor dynamics govern the macroscopic electrical response remains insufficiently understood. Here, $K(NaPr)_{1-x}(SrBa)_xNb_5O_{15}$ ceramics with continuously varying configurational entropy were designed to investigate the origin of relaxor-ferroelectric evolution. With increasing Sr/Ba substitution, the electrical response evolves from an ergodic-relaxor state with slim hysteresis loops and four current peaks to a ferroelectric-like state with double current peaks, fatter loops, and increased remanent and maximum polarizations. This evolution is accompanied by increased lattice parameter *c* and tetragonality (*c*/*a*), indicating a structural evolution toward a more stable polar state. The dielectric anomalies and Vogel-Fulcher analysis further reveal an increase in freezing temperature and a decrease in activation energy, indicating strengthened coupling among polar nanoregions and a gradual evolution from the relaxor state toward a non-ergodic relaxor or ferroelectric state. Notably, this trend is opposite to the commonly expected enhancement of relaxor behavior in high-entropy systems, suggesting that configurational entropy does not simply strengthen relaxor characteristics through increased compositional disorder. Instead, configurational entropy modulates the order-disorder state of A-site occupation, thereby changing the octahedral tilting patterns and the modulation structure, which affects the diffuseness of the phase transition. These results demonstrate that the macroscopic electrical response in the high-entropy $K(NaPr)_{1-x}(SrBa)_xNb_5O_{15}$ system is regulated by crystal structure, modulation structure, and polar nanoregion dynamics, providing new insight into the relaxor behavior of TTB ferroelectrics.

Keywords: tetragonal tungsten bronze; high entropy; relaxor ferroelectrics; incommensurate modulation

1 Introduction

Relaxor ferroelectrics are a class of disordered crystals with distinctive structural and functional characteristics [1]. Unlike normal ferroelectrics, which typically exhibit sharp phase-transition peaks, relaxor ferroelectrics are characterized by a broadened dielectric peak and pronounced frequency dispersion, with the dielectric maximum generally shifting toward higher temperatures as the frequency increases [2,3]. This polarization behavior arises from the disruption of long-range ferroelectric order by structural disorder, so that polarization correlations are retained only on a local scale, leading to the formation of polar nanoregions (PNRs). Site occupancy disorder, charge disorder, and ionic-size disorder can all promote the emergence of the polar nanoregions [4]. Owing to these unique features, relaxor ferroelectrics exhibit excellent physical properties, including large dielectric tunability, high dielectric permittivity, significant electric-field-induced strain, as well as strong electro-optic and photorefractive effects [5]. These properties make them promising candidates for microwave tunable devices, high-energy-density energy storage capacitors, solid-state cooling systems, piezoelectric sensors and actuators [6–9].

The high-entropy strategy, through the synergistic effects of entropy-dominated phase stabilization, lattice distortion, sluggish diffusion, and multicomponent interactions, can effectively regulate structural disorder and local polarization behavior [10,11]. It is therefore expected to serve as an effective approach for designing relaxor ferroelectrics. Unlike conventional doping strategies, which are often limited by solid solubility, high-entropy design allows a high degree of atomic substitution, enabling flexible compositional configuration and tunable functional properties [12]. By introducing multiple cations to construct high-entropy systems, the enhanced compositional heterogeneity generally induces local structural disorder and polar fluctuations, thereby disrupting long-range ferroelectric order and promoting relaxor behavior. In the field of energy storage, this strategy has been widely adopted to improve energy storage density and efficiency [13–16].

However, the effect of high entropy on relaxor behavior is not always positive. Some studies have shown that relaxor behavior may be absent in certain high-entropy systems, accompanied instead by enhanced ferroelectricity [17,18]. This phenomenon suggests that high entropy does not enhance relaxor behavior through compositional disorder alone, but may also involve more complex local-structure evolution.

Among various ferroelectric systems, tetragonal tungsten bronze (TTB) oxides, with flexible site occupancy and compositional diversity, provide an ideal structural platform for exploring the relationship between high-entropy design and relaxor behavior. The general formula of the TTB structure is $(A2)_4(A1)_2(B1)_2(B2)_8(C)_4(X)_{30}$. Its crystal framework consists of ten corner-sharing BO_6 octahedra, forming three types of interstitial sites: quadrangular A1, pentagonal A2, and triangular C sites. Depending on the site occupancy, TTB compounds can be classified as stuffed, filled, unfilled, or empty structures [19]. The diverse A-site environments and variable occupancies enable TTB systems to accommodate cations with different ionic radii and valence states, resulting in broad tunability of crystal structure, local polarization, and macroscopic electrical properties. Accordingly, TTB ceramics exhibit rich dielectric, ferroelectric, pyroelectric, photoelectric, and piezoelectric responses and have shown great potential in energy storage, sensing/actuation, energy conversion, infrared detection, and optoelectronic devices [20–23].

Understanding the origin of dielectric relaxation and regulating the relaxor-ferroelectric crossover in TTB systems remain important issues in materials science and condensed-matter physics [24]. In TTB compounds, polarization mainly arises from the off-center displacement of B-site cations within BO_6 octahedra along the [001] direction, while A-site cations modulate the tilting and distortion of the BO_6 framework through different A–O bonding environments [25,26]. These local distortions can be spatially organized into commensurate or incommensurate modulation structures.

Commensurate modulation generally reflects stronger long-range structural coherence and cooperative polarization, whereas incommensurate modulation is often closely associated with relaxor behavior [27]. Thus, modulation structures provide a key structural perspective for linking local lattice distortion with macroscopic dielectric relaxation. However, the formation of modulation structures also complicates crystallographic analysis, making TTB compounds less well understood than perovskite ferroelectrics [28]. This complexity is further amplified in multicomponent high-entropy TTB systems, where configurational entropy, site occupation, local distortion, and modulation behavior are intrinsically coupled. Therefore, clarifying the evolution of modulation structures is crucial for understanding the factors that govern relaxor behavior in high-entropy TTB ferroelectrics.

In this work, a series of entropy-tunable tetragonal tungsten bronze ceramics, $K(NaPr)_{1-x}(SrBa)_xNb_5O_{15}$ with x = 0.1, 0.3, 0.4, 0.5, 0.6, 0.7, and 0.8, denoted as N10x, were constructed through A-site Sr/Ba co-substitution. Unlike previous reports on single high-entropy compositions, the N10x series shows continuous variations in composition and configurational entropy, enabling a more systematic analysis of the multiple factors in high-entropy TTB systems. As illustrated in **Fig. 1**, this work proposes a mechanism framework to decouple the effects of configurational entropy, crystal structure, relaxor dynamics, local structural distortion, and modulation-structure evolution on diffuse phase transition and relaxor-ferroelectric evolution. This study provides insight into the regulation of modulation structures and relaxor behavior in high-entropy TTB systems, offering guidance for the rational design of TTB relaxor ferroelectrics.

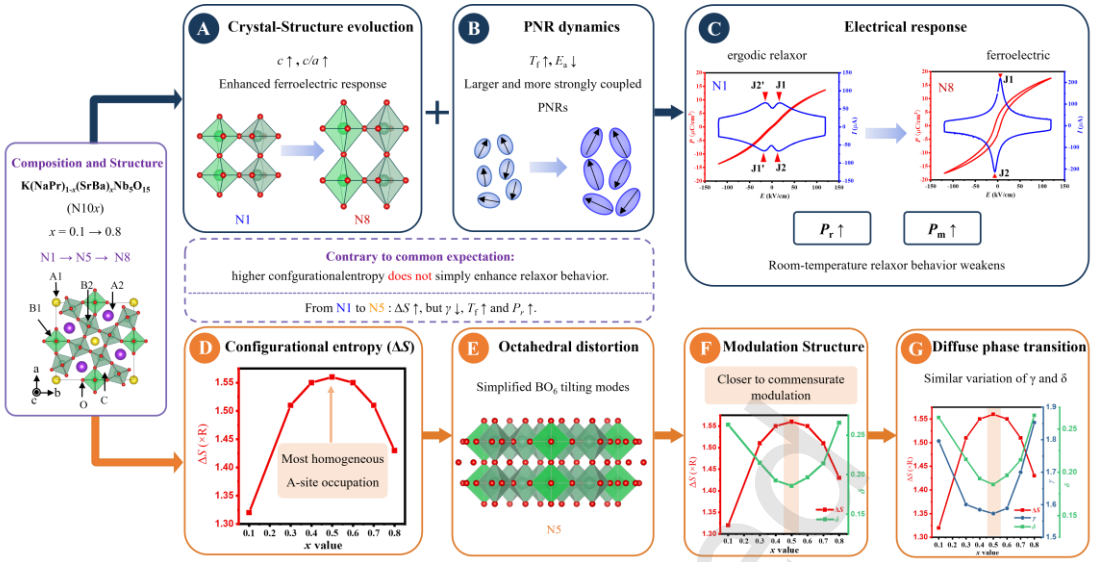

Fig. 1 Schematic illustration of the decoupling of multiple factors affecting diffuse phase transition and relaxor-ferroelectric evolution in high-entropy TTB ceramics.

2 Experimental

$K(NaPr)_{1-x}(SrBa)_xNb_5O_{15}$ ceramics (x = 0.1, 0.3, 0.4, 0.5, 0.6, 0.7 and 0.8, denoted as N10x) were prepared by a conventional solid-state reaction method using K_2CO_3 (99.99%, Aladdin), Na_2CO_3 (99.5%, Aladdin), Pr_6O_{11} (99.9%, Rare-Chem), $SrCO_3$ (99.95%, Aladdin), $BaCO_3$ (99.95%, Aladdin), Nb_2O_5 (99.99%, Aladdin), and $MnCO_3$ (99.95%, Aladdin) as starting materials. The powders were weighed according to the nominal stoichiometry and ball-milled in ethanol with zirconia balls at 300 rpm for 4 h. The resulting slurry was dried at 80 °C for 2 h, and the dried powders were sieved through a 60-mesh screen, followed by calcination in an alumina crucible at 1200 °C for 4 h to obtain the target ceramic powders. After calcination, 2.5 mol% $MnCO_3$ was added, and the powders were subjected to a second ball-milling, drying, and sieving process. $MnCO_3$ was introduced as a sintering aid to promote densification and increase resistivity [29], and thus Mn was not included in the nominal formula or configurational entropy calculation. The calcined powders were then mixed with polyvinyl butyral (PVB), granulated, and uniaxially pressed into pellets with a diameter of 8 mm. The green pellets were

placed between zirconia setter plates, heated at 600 °C for 4 h to remove the organic binder, and then sintered at 1200-1300 °C for 2 h.

Phase composition and crystal structure were characterized by X-ray diffraction (XRD; D8 Advance, Bruker, Karlsruhe, Germany) using Cu Kα radiation. Raman spectra were collected from polished ceramic surfaces using a confocal Raman spectrometer (Alpha 300S, WITec, Germany) equipped with a 532 nm Nd/YAG laser. The microstructure was examined by scanning electron microscopy (SEM; MERLIN VP Compact, Carl Zeiss, Germany). For SEM observation, the samples were polished and thermally etched for 30 min at a temperature 100 °C below the sintering temperature. The grain size was measured using Nano Measure software. Selected-area electron diffraction (SAED) patterns were acquired by transmission electron microscopy (TEM; Tecnai G2 F20, FEI, USA) operated at 200 kV and recorded with a Gatan OneView 4K × 4K fast camera.

The dielectric properties in the temperature range of -100 to 175 °C were measured using a precision LCR meter (E4980A, KEYSIGHT, USA) combined with a high-temperature dielectric measurement system (DMS-2000, Partulab Technology, China). The dense sintered ceramic pellets were ground with sandpaper to a thickness of 0.15 mm, and Ag electrodes with a diameter of 3 mm were subsequently deposited by magnetron sputtering (MSP-300BT, Chuangshiweina Technology Co., Ltd., China). The samples with sputtered Ag electrodes were then subjected to polarization-electric field (*P*-*E*) hysteresis loop and current-electric field (*I*-*E*) measurements at 10 Hz using a ferroelectric analyzer (TF Analyzer 1000, aixACCT, Germany).

3 Results and Discussion

3.1 Microstructure and phase composition

Figs. 2(a-c) and S1 show the surface morphologies of samples with different compositions (N1-N8) after polishing and thermal etching, and the insets present the corresponding grain-size distributions. All samples exhibit clear grain boundaries and high densification. Because of the pronounced difference between the lattice parameters *a* and *c* in the tetragonal tungsten bronze structure, grain growth shows a strong preferred orientation. The higher growth rate along the (001) plane leads to the formation of typical rod-like grains [30]. With increasing Sr/Ba content, the optimum sintering temperature gradually increases from 1200 °C for N1 to 1300 °C for N8. Meanwhile, the average grain size also increases slightly, as shown in **Fig. 2(d)**.

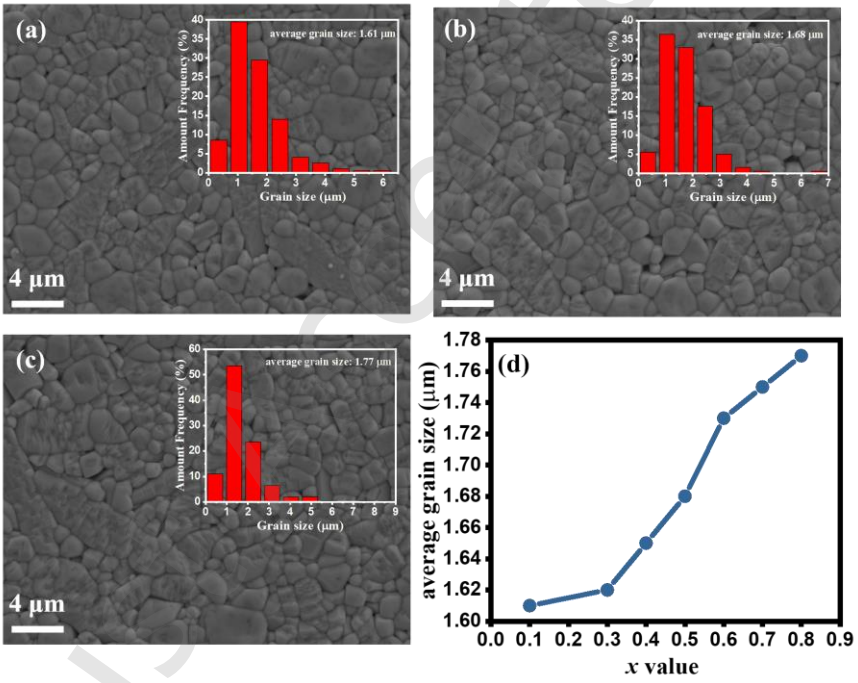

Fig. 2 SEM photographs of the N10*x* ceramics: (a) N1, (b) N5, (c) N8. The insets show the corresponding grain-size distributions. (d) Average grain size as a function of *x*.

The X-ray diffraction (XRD) patterns in **Fig. 3(a)** show that all compositions crystallize as a single TTB phase with the *P*4/*mbm* space group (PDF #07-0314), and no secondary phases are observed. This result indicates that Sr and Ba are fully incorporated into the lattice. Because Sr^{2+} and Ba^{2+} have larger ionic radii than the substituted Na^{+} and Pr^{3+}, the unit cell expands with increasing doping level.

As a result, diffraction peaks such as the (311) reflection shift continuously toward lower angles, as shown in **Fig. 3(b)**. To further analyze the crystal structure, Rietveld refinement was performed using the FullProf program (**Fig. S2**). Since laboratory XRD cannot reliably distinguish subtle distortions caused by octahedral tilting/twisting or B-site cation off-centering, all compositions were refined using the *P*4/*mbm* space group [29]. The lattice parameters, cell volume, and tetragonality (*c*/*a*) calculated from the XRD data are summarized in **Fig. 3(c)**. Their monotonic increase provides direct crystallographic evidence for the successful substitution of Sr and Ba and explains the observed peak shifts.

Of particular interest, the (420) and (311) reflections near 32°, as well as the (002) and (620) reflections near 46°, gradually merge into single peaks when the doping level reaches $x = 0.6$ (N6). This peak-merging behavior suggests an increase in tetragonality (*c*/*a*), consistent with the XRD analysis. In unfilled TTB systems, reduced tetragonality has been reported to disturb the off-center displacement of ferroelectrically active B-site cations within the BO_6 octahedra, thereby suppressing ferroelectric order and promoting relaxor behavior [26]. By contrast, the increased *c*/*a* observed in the present work suggests enhanced tetragonal distortion, which may help stabilize the B-site off-center displacement. Meanwhile, the expansion along the polar *c* axis, reflected by the increased lattice parameter *c*, provides a higher *c*/*a* and thus favors ferroelectric polarization [31]. Given the strong structural anisotropy ($a = b \gg c$) of N10x ceramics, polarization switching from the *c*-axis to the *a*-/*b*-axis is thermodynamically unfavorable, indicating the predominant existence of 180° domains [32–34]. Overall, these structural features are expected to weaken the relaxor character and enhance the polarization response, providing a structural basis for the relaxor-ferroelectric transition illustrated in **Fig. 1**.

To further probe the local structural evolution induced by Sr/Ba substitution, room-temperature Raman spectra were collected for all samples, as shown in **Fig. 3(d)**. The Raman bands below 200 cm^{-1} are assigned to vibrations of the A-site cations, those in the 200–400 cm^{-1} region correspond to the bending vibrations of O–B–O bonds within the BO_6 octahedra, and the bands above 400 cm^{-1} originate from the stretching vibrations of B–O bonds [31]. With increasing Sr/Ba substitution, the Raman modes gradually shift toward lower wavenumbers, directly indicating lattice expansion and increased average bond length, in good agreement with the XRD results. Notably, the two Nb–O stretching modes near 600 cm^{-1} progressively merge and become narrower as the substitution level increases, suggesting that the distortion of the BO_6 octahedra, especially within the *ab* plane, is gradually alleviated [35,36]. In TTB compounds, stronger octahedral distortion usually gives rise to more complex local structural fluctuations, which disrupt the development of long-range polarization and instead favor the formation of localized polar regions, thereby enhancing relaxor behavior. Therefore, the peak narrowing observed here implies reduced local structural heterogeneity of the BO_6 octahedra, which is expected to be favorable for an enhanced polarization response.

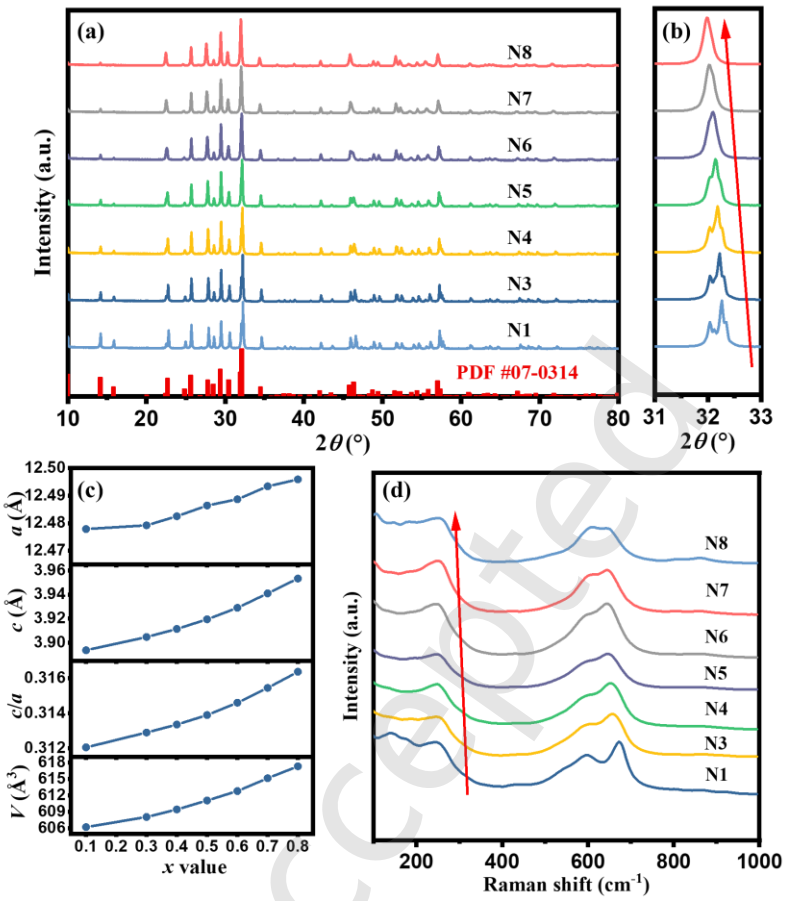

Fig. 3 (a) XRD patterns of the N10*x* ceramics. (b) Enlarged view of the diffraction peaks. (c) Lattice parameters, tetragonality (*c*/*a*), and cell volume of the N10*x* ceramics. (d) Raman spectra of the N10*x* ceramics.

3.2 Polarization and switching behavior

On the basis of the above microstructural and crystal-structure evolution, the macroscopic polarization and switching behaviors of the N10*x* ceramics were further investigated by polarization-electric field (*P*-*E*) hysteresis loops and current-electric field (*I*-*E*) curves. **Figs. 4 and S3** present the *P*-*E* loops and *I*-*E* curves of the N10*x* ceramics measured at room temperature under an electric field of 120 kV/cm. As shown in **Figs. 4(a-b)** and **S3(a-b)**, samples N1-N5 exhibit slim *P*-*E* hysteresis loops, accompanied by *I*-*E* curves with four distinct current peaks (J1, J2, J1′, and J2′). Although four current peaks are

also commonly observed in antiferroelectrics with double hysteresis loops due to reversible antiferroelectric-ferroelectric phase transitions, the characteristic transition peaks J1 and J2 usually occur at different electric fields. In the present work, however, J1 and J2 of samples N1-N5 occur at nearly the same electric field. Specifically, J1 corresponds to the electric-field-induced transition from the relaxor state to the ferroelectric state, whereas J2 arises from the spontaneous recovery of the induced ferroelectric state back to the initial relaxor state upon field removal. The same process occurs under a reverse electric field, leading to the corresponding peaks J1' and J2'. This reversible relaxor-ferroelectric phase transition suggests that samples N1-N5 are in an ergodic relaxor state at room temperature. Notably, under the same electric field, the current peaks gradually shift toward lower fields and their intensities increase with increasing Sr/Ba substitution (**Fig. S4(a)**). These results indicate that Sr/Ba substitution progressively destabilizes the relaxor state, thereby facilitating the electric-field-induced transition to the ferroelectric state. At the same time, the enhanced peak intensity suggests that more PNRs are involved in the switching process and respond more cooperatively.

When the substitution level reaches $x = 0.6$, the *I-E* curves exhibit ferroelectric-like characteristics, showing only two current peaks in the first and third quadrants, while the corresponding peak fields remain relatively low (**Figs. 4(c-d) and S3(c)**). Such a pronounced evolution in the macroscopic electrical response suggests that Sr/Ba substitution has markedly altered the microscopic polarization dynamics, which will be discussed in detail in Section 3.3. In addition, Sr/Ba substitution leads to a continuous increase in the maximum polarization (P_m), and the remanent polarization (P_r) also shows a marked increase when the substitution level reaches $x = 0.5$, as shown in **Fig. S4(b)**. These results indicate a progressive weakening of the relaxor character and an enhancement of the ferroelectric response with increasing Sr/Ba substitution. This behavior is in good agreement with the structural analysis in Section 3.1, where the increases in the lattice parameter c and tetragonality (c/a), together

with the Raman evidence for a more uniform local BO_6 environment, all suggest a structural evolution favorable for enhancing the ferroelectric response.

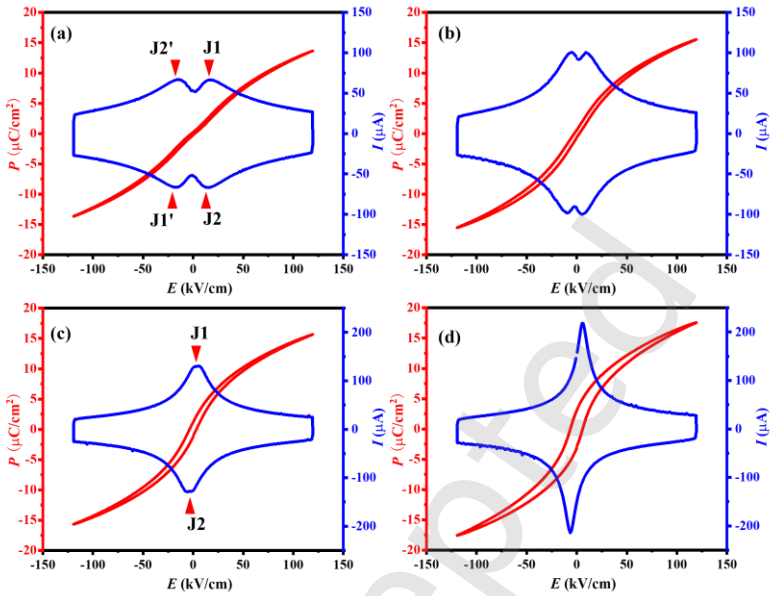

Fig. 4 *P-E* loops and *I-E* curves of the N10*x* ceramics: (a) N1, (b) N5, (c) N6, (d) N8.

3.3 PNR-driven relaxor-ferroelectric transition

To further understand the evolution of the macroscopic ferroelectric properties with Sr/Ba substitution, the dielectric spectra of the N10*x* ceramics were systematically investigated as a function of temperature over the frequency range of 100 Hz-1 MHz, as shown in **Figs. 5(a-d) and S5**. The dielectric spectra exhibit two distinct dielectric anomalies (**Fig. 5(a)**). The high-temperature Curie peak (T_c), corresponding to the ferroelectric phase transition, shows almost no frequency shift but displays noticeable broadening, indicating the diffusive nature of the phase transition. The second anomaly is a low-temperature relaxation peak (T_s), commonly observed in TTB compounds, which is closely related to the order-disorder distribution of A-site cations [37]. It exhibits pronounced frequency dispersion and shifts toward higher temperatures with increasing frequency. With increasing Sr/Ba substitution, the low-temperature relaxation peak gradually moves to higher temperatures and progressively merges with the high-temperature diffuse phase-transition peak (**Figs. 5(b-c) and S5(a-**

b)). However, when the substitution level reaches x = 0.7 (N7), the high-temperature diffuse phase-transition peak (T_c) reappears and becomes more intense than the low-temperature relaxation peak, as shown in **Figs. 5(d) and S5(c)**. Meanwhile, both the lattice parameter c and tetragonality (c/a) continue to increase, indicating a structural evolution toward a more stable polar state with enhanced ferroelectric polarization. As a result, the relaxor behavior is gradually weakened, whereas the ferroelectric response becomes strengthened, leading to the reappearance of T_c. This evolution is consistent with the macroscopic ferroelectric behavior discussed above, where N7 and N8 exhibit noticeably fatter *P-E* hysteresis loops together with increased remanent polarization (P_r) and maximum polarization (P_m).

To gain further insight into the relaxor nature of the N10x ceramics, the frequency-dispersion behavior of the low-temperature relaxation peak T_s, associated with the dynamic evolution of polar nanoregions (PNRs), was quantitatively analyzed using the Vogel-Fulcher equation (**Eq. (1)**)[3]:

$$f = f_0 \exp\left[-\frac{E_a}{k_B(T_m - T_f)}\right] \quad (1)$$

where f is the measurement frequency, f_0 is the attempt frequency, E_a is the activation energy, k_B is the Boltzmann constant, T_m corresponds to the temperature of the relaxation peak T_s, and T_f is the freezing temperature of polar nanoregions. Because the T_s peak in N7 and N8 is relatively weak and strongly overlaps with the high-temperature anomaly, the two contributions cannot be reliably separated. Therefore, Vogel-Fulcher fitting was performed only for N1-N6, as shown in **Fig. 5(e)**. The experimental data can be well fitted by the Vogel-Fulcher relation, indicating that the low-temperature relaxation in the N10x ceramics is characteristic of a spin-glass-like polarization freezing process. The fitted parameters are summarized in **Table 1**. With increasing Sr/Ba substitution, the freezing temperature T_f increases monotonically from -64 °C to -15 °C, while the activation energy E_a decreases monotonically from 0.0973 eV to 0.0705 eV. The increase in T_f indicates that the interactions among PNRs are progressively strengthened, causing them to freeze at higher temperatures. In the Vogel-

Fulcher model, E_a represents the effective activation energy barrier for thermally activated relaxation or reorientation of PNRs/polar clusters [38,39]. A higher E_a implies that PNRs are more strongly constrained by local random fields and structural heterogeneity, making cooperative alignment more difficult; this typically gives rise to slimmer hysteresis loops and higher energy-storage efficiency, as the formation of stable long-range ferroelectric order is suppressed [40]. In the present work, the decrease in E_a suggests a reduced energy barrier for PNR reorientation, indicating enhanced coupling among PNRs. Under an external electric field, such stronger coupling promotes a more cooperative response of PNRs, allowing a larger number of PNRs to participate in field-induced alignment and thereby leading to higher current peaks in the *I-E* curves. Meanwhile, the field-induced polarization state becomes less reversible after removal of the electric field, which is consistent with the increase in remanent polarization and the broadening of the hysteresis loops.

This interpretation can be further understood using the ferroelectric microdomain model of relaxor ferroelectrics. According to this model, PNRs begin to form at the Burns temperature T_B during cooling [41]. T_B is defined as the temperature at which the dielectric response starts to deviate from the Curie-Weiss law, and is generally regarded as the boundary between the paraelectric state and the ergodic relaxor state. For the N10*x* system, T_B was determined from the temperature at which the linear $1/\varepsilon_r$–*T* relationship begins to deviate from the Curie-Weiss law ($\varepsilon_r = C/(T - T_0)$, *C* is the Curie constant and T_0 is the Curie-Weiss temperature) [33], as shown in **Fig. 5(f)**, and the corresponding values are listed in **Table 1**. In the temperature range between T_B and T_f, the PNRs remain dynamically reversible, corresponding to the ergodic relaxor state. The freezing temperatures T_f and *I-E* curves of N1-N5 consistently indicate that these samples remain in an ergodic relaxor state at room temperature. With increasing Sr/Ba substitution, T_f continuously shifts toward higher temperatures, while the ergodic relaxor temperature interval (T_B–T_f) gradually narrows. This indicates strengthened coupling among PNRs. As listed in **Table 1**, the T_f value of N6 already approaches 0 °C. Based on the monotonic

increase in T_f, it is reasonable to infer that the freezing temperatures of N7 and N8 approach room temperature. Therefore, these highly substituted samples tend to deviate from the ergodic relaxor state at room temperature. Their PNRs become more strongly coupled and gradually grow into long-range-ordered ferroelectric domains. Under an applied electric field, such domains are more likely to undergo irreversible switching, giving rise to the ferroelectric-like double current peaks in the *I-E* curves. Combined with the decrease in E_a, these results indicate that Sr/Ba substitution drives the PNRs from a highly dynamic and weakly coupled state toward a more strongly correlated and less reversible state, thereby weakening the relaxor character and enhancing the ferroelectric response. This evolution is schematically summarized in **Fig. 1** as a transition from a dynamic relaxor state to a more stable ferroelectric state.

To quantify the diffuseness of the phase transition, the dielectric spectra measured at 1 MHz were fitted using the modified Curie-Weiss law (**Eq. (2)**)[33]:

$$\frac{1}{\varepsilon_r} - \frac{1}{\varepsilon_m} = \frac{(T - T_m)^\gamma}{C} \tag{2}$$

where ε_m is the maximum dielectric constant, T_m is the temperature corresponding to the dielectric maximum, C is a constant, and γ is the diffuseness coefficient. The fitting results are shown in **Fig. 5(g)**, and the composition dependence of γ summarized in **Fig. 5(h)**. In general, $\gamma = 1$ corresponds to a normal ferroelectric with a sharp dielectric peak, whereas a larger γ indicates a higher degree of phase-transition diffuseness. All samples exhibit γ values greater than 1, confirming the diffuse nature of the phase transition throughout the whole composition range. With increasing Sr/Ba substitution, γ first decreases from N1 to N5 and then increases again toward N8, showing a U-shaped variation. This nonmonotonic evolution suggests that the diffuseness of the phase transition is not governed by the substitution level alone, but may involve the effects of modulation-structure evolution and configurational entropy. Since modulated structures are widely present in tungsten bronze compounds

[28,42,43], the relationship among modulation structure, configurational entropy, and γ will be further discussed in the following section.

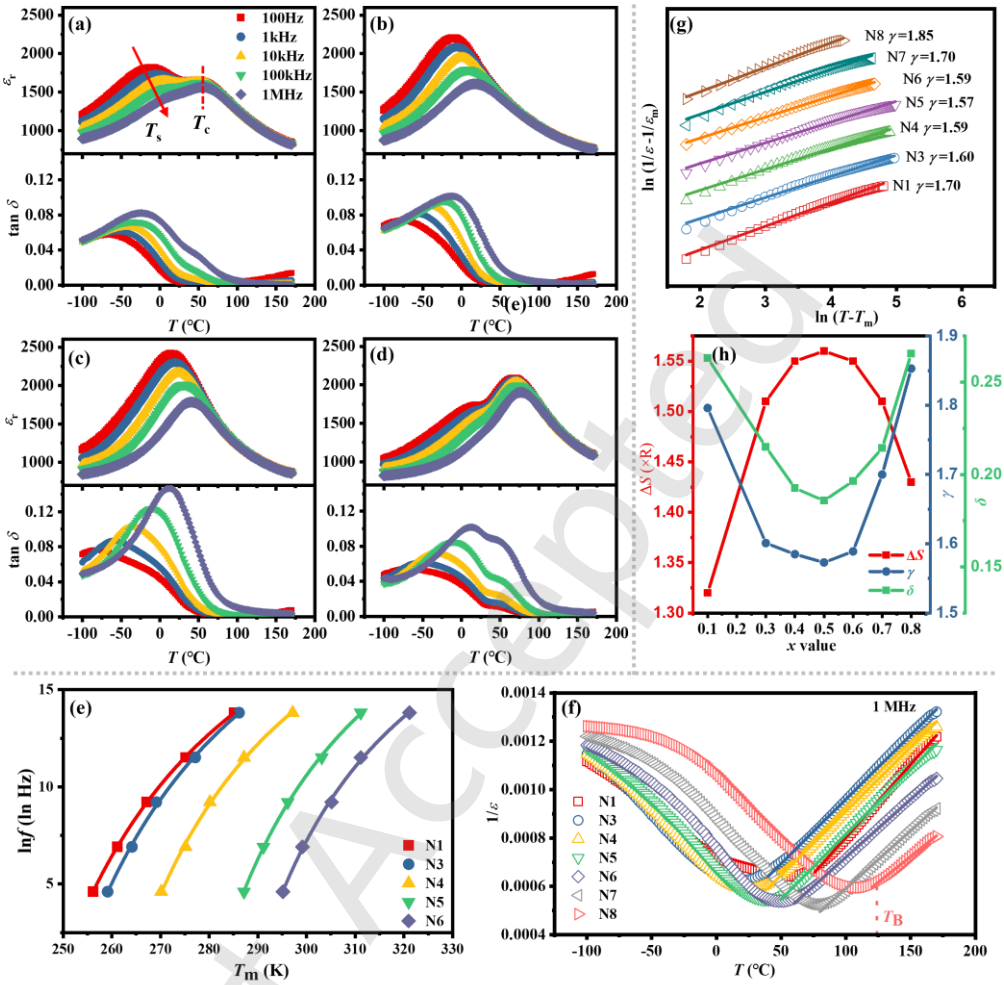

Fig. 5 Temperature dependence of dielectric permittivity and dielectric loss of the N10x ceramics: (a) N1, (b) N3, (c) N5, (d) N7. (e) Frequency dependence of the relaxation-peak temperature T_s, where the symbols are the experimental data and the solid lines are the Vogel-Fulcher fitting results. (f) Temperature dependence of $1/\varepsilon_r$, where the solid lines represent the Curie-Weiss fitting results. (g) Plots of ln $(1/\varepsilon_r - 1/\varepsilon_m)$ versus ln $(T - T_m)$ at 1 MHz, where the solid lines represent the fitting results. (h) Composition dependence of configurational entropy ΔS, diffuseness coefficient γ, and incommensurability parameter δ.

Table 1. Vogel-Fulcher fitting results for the dielectric relaxation behavior of N10*x* ceramics

Sample	N1	N3	N4	N5	N6
T_f (°C)	-64	-59	-44	-24	-15
E_a (eV)	0.0973	0.0948	0.0836	0.0768	0.0705
f_0 (Hz)	3.01×10^{12}	4.44×10^{12}	1.65×10^{12}	1.76×10^{12}	4.78×10^{12}
T_B (°C)	78	42	38	48	62
(T_B−T_f) (°C)	142	101	82	72	77

3.4 Configurational entropy-regulated modulation-structure evolution

Selected-area electron diffraction (SAED) is an effective technique for revealing the local modulation characteristics of TTB structures. The SAED patterns of the N10*x* ceramics along the [110] zone axis are shown in **Figs. 6 and S6**. In addition to the fundamental diffraction spots of the TTB structure, distinct incommensurate satellite reflections can be clearly observed along the $[1\bar{1}0]$ direction, as marked by the red dashed lines in **Figs. 6(a-d)**. The positions of these reciprocal-lattice spots can be described by the reciprocal vector $H = ha^* + kb^* + lc^* + mk^*$, where a^*, b^*, and c^* are the basis vectors of the reciprocal lattice, and mk^* represents the incommensurate diffraction spots, with the integer *m* denoting the diffraction order. The incommensurate modulation wave vector *k** is expressed by **Eq (3)** [19]:

$$k^* = \pm\left[\frac{1}{4}(1+\delta)(\mathrm{a}^* + \mathrm{b}^*) + \frac{1}{2}\mathrm{c}^*\right] \quad (3)$$

$$\delta = \frac{y-x}{y+x} \quad (4)$$

where *x* and *y* are the distances between adjacent incommensurate diffraction spots, as shown in **Fig. 6(a)**. The incommensurability parameter δ (defined in **Eq. (4)**) is used to quantify the deviation of the modulation structure from the commensurate state. When δ = 0, the structure corresponds to a commensurate modulation state, which is generally associated with long-range order and normal

ferroelectric behavior [44,45]. In contrast, a nonzero δ indicates an incommensurate modulation structure, which is generally associated with A-site cation disorder and oxygen-octahedral distortion [25,27]. Interestingly, δ exhibits a U-shaped dependence on x, decreasing from 0.263 for N1 to 0.186 for N5 and then increasing to 0.265 for N8 (**Fig. 5(h)**).

This U-shaped variation of δ is consistent with that of the diffuseness coefficient γ, suggesting that the diffuse phase-transition behavior is closely associated with the modulation structure. Structural modulation reflects the spatial organization of oxygen-octahedral tilting and distortion, which can influence the distribution of local transition temperatures through its coupling with the polar displacement of B-site cations [25,26]. A smaller δ means that the modulation state is closer to the commensurate state, whereas a larger δ reflects a greater deviation from the commensurate state. Under the latter condition, the orientational disorder of polar off-centering at the low-symmetry B2 sites becomes more pronounced, and its coupling with the polar displacement of cations at the high-symmetry B1 sites becomes weaker [24]. As a result, the cooperative nature of the phase transition is reduced, and different local regions tend to undergo polarization switching over a wider temperature range. This gives rise to a broader distribution of local transition temperatures and thus a larger γ.

To further understand the evolution of the modulation structure, the configurational entropy (ΔS) was calculated via **Eq. (5)** [45]:

$$\Delta S = -R\left[\left(\sum_{i=1}^{N} x_{\mathrm{i}}\, lnx_{\mathrm{i}}\right)_{\mathrm{cation-sit}} + \left(\sum_{j=1}^{M} x_{\mathrm{j}}\, lnx_{\mathrm{j}}\right)_{\mathrm{anion-sit}}\right] \quad (5)$$

where x_{i} and x_{j} are the molar fractions of the constituent elements at the cation and anion sites, respectively, and R is the universal gas constant. As shown in **Fig. 5(h)**, ΔS exhibits an inverted-U-shaped dependence on composition and reaches a maximum value of 1.56R at N5. Notably, this trend is opposite to that of δ. In TTB oxides, A-site cations affect the tilting and distortion of oxygen octahedra through different A–O bonding states, thereby giving rise to either incommensurate or

commensurate structural modulation [26]. The incommensurate structure is considered to arise from a mixture of distinct octahedral tilting patterns [24]. In the present system, increasing configurational entropy statistically homogenizes the A-site occupation environment and reduces the effective difference between the A1 and A2 sites. As a result, the diversity of octahedral tilting and twisting modes is reduced, favoring a modulation state closer to the commensurate limit and thus giving rise to the reduced δ around N1-N5. Upon further Sr/Ba substitution, the configurational entropy decreases, while the compositional and structural bias of the lattice becomes stronger again, leading to a larger δ.

Since γ follows the same U-shaped variation as δ, the diffuseness coefficient γ is negatively correlated with ΔS in the present system. This result deviates from the common empirical expectation that higher configurational entropy should induce stronger disorder and thus a more diffuse phase transition. In addition, from N1 to N5, the increase in ΔS is accompanied by an increased freezing temperature (T_f) and enhanced remanent polarization (P_r), indicating that the room-temperature relaxor behavior is not strengthened with increasing entropy. Therefore, as summarized schematically in **Fig. 1**, configurational entropy does not directly determine the relaxor characteristics in this system, but mainly influences the diffuse phase-transition behavior through its regulation of the modulation structure. Meanwhile, the increased c/a and more uniform BO_6 environment provide a structural basis for the ferroelectric response, and the increased T_f together with the decreased E_a further indicates strengthened PNR coupling, which drives the relaxor-ferroelectric evolution.

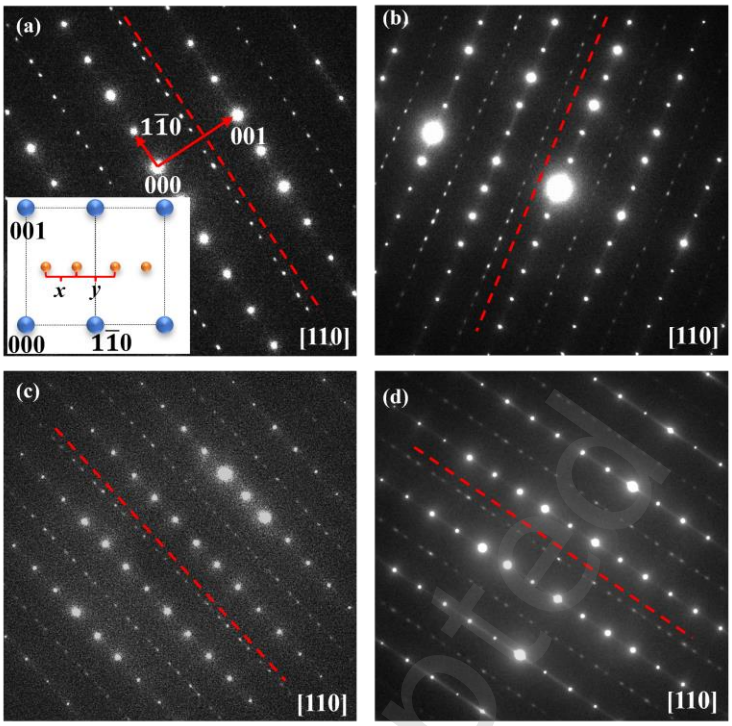

Fig. 6 SAED patterns of the N10*x* ceramics along the [110] zone axis: (a) N1, (b) N3, (c) N5, (d) N7. The inset in (a) shows a schematic illustration of the diffraction pattern, where the blue circles represent basic diffraction, the orange circles represent first-order incommensurate diffraction, and *x* and *y* represent the distances between adjacent satellite diffraction spots.

4 Conclusions

$K(NaPr)_{1-x}(SrBa)_xNb_5O_{15}$ ceramics were synthesized by the conventional solid-state reaction method. The coupling among configurational entropy, incommensurate modulation, dielectric relaxation and macroscopic electrical response of $KNaPrNb_5O_{15}$-based tetragonal tungsten bronze (TTB) ceramics was systematically investigated. Sr/Ba substitution continuously increases the lattice parameter *c* and tetragonality (*c*/*a*), while Raman results indicate a progressively more uniform local BO_6 environment, revealing a structural evolution favorable for ferroelectric polarization. Correspondingly, the macroscopic electrical response evolves from slim *P*-*E* loops with four current peaks in N1-N5, characteristic of an ergodic relaxor state with reversible relaxor-ferroelectric transition, to ferroelectric-like behavior in N6-N8 with double current peaks and fatter *P*-*E* loops. Dielectric and

Vogel-Fulcher analyses show that Sr/Ba substitution strengthens the coupling among polar nanoregions, as evidenced by the increased freezing temperature and reduced activation energy, thereby reducing the reversibility of field-induced polarization switching and driving the evolution from relaxor to ferroelectric response.

Besides, configurational entropy modifies the statistical distribution of A-site occupation, thereby changing the octahedral tilting patterns and the deviation of the modulation state from the commensurate limit. The evolution of the modulation structure further affects the diffuseness of the phase transition, as reflected by the variation of the diffuseness coefficient γ. Notably, although Sr/Ba substitution initially increases the configurational entropy, the room-temperature relaxor behavior gradually weakens and the ferroelectric response becomes enhanced, which is opposite to the commonly expected enhancement of relaxor behavior in high-entropy systems. This finding suggests that configurational entropy does not simply promote relaxor characteristics through increased compositional disorder, but instead mainly affects modulation structure and diffuse phase-transition behavior. Overall, this work provides a mechanistic understanding of how configurational entropy, crystal structure, modulation structure, and PNR dynamics regulate diffuse phase transition and relaxor-ferroelectric evolution in TTB ceramics, and offers a theoretical basis for designing lead-free dielectric materials with relaxor properties.

Acknowledgements

This work was supported by the Tsinghua University State Key Laboratory of New Ceramic Materials Project (Grant No. 2025QHTC-ZZKYB002).

Author contributions

Chongyang Zhang: Writing – original draft, Validation, Methodology, Investigation, Formal analysis, Data curation, Conceptualization. **Weijia Guo:** Writing – review and editing, Validation, Methodology, Investigation, Formal analysis, Data curation. **Xingchen Zhang:** Methodology, Investigation, Formal analysis, Data curation. **Bowen Yin:** Methodology, Formal analysis, Data curation. **Yutian Lu:** Validation, Methodology, Formal analysis, Data curation. **Hui Zhang:** Methodology, Formal analysis, Data curation. **Zhenxing Yue:** Writing – review & editing, Validation, Supervision, Resources, Project administration, Conceptualization, Funding acquisition.

Availability of data and materials

The data that support the findings of this study are available from the corresponding author upon reasonable request.

Competing interests

The authors have no competing interests to declare that are relevant to the content of this article.

References

[1]Bokov AA, Ye ZG. Recent progress in relaxor ferroelectrics with perovskite structure. *J Mater Sci* 2006, **41**: 31–52.

[2]Cross LE. Relaxor ferroelectrics. *Ferroelectrics* 1987, **76**: 241–267.

[3]Viehland D, Jang SJ, Cross LE, *et al.* Freezing of the polarization fluctuations in lead magnesium niobate relaxors. *J Appl Phys* 1990, **68**: 2916–2921.

[4]Shvartsman VV, Lupascu DC. Lead-Free Relaxor Ferroelectrics. *J Am Chem Soc* 2012, **95**: 1–26.

[5] Jiang QH, Zhao WG, Zhang M, *et al.* Dynamic Atomistic Polar Structure Underpins Ultrahigh Linear Electro-Optic Coefficient in Transparent Ferroelectric Ceramics. *J Am Chem Soc* 2025, **147**: 42909–42917.

[6] Dan YJ, Tang LP, Ning WZ, *et al.* Achieving enhanced energy storage performance and ultra-fast discharge time in tungsten–bronze ceramic. *J Adv Ceram* 2024, **13**: 1349–1358.

[7]Wu ZX, Hu WT, Banerjee K, *et al.* Enhanced electrocaloric effect in lead-free relaxor ferroelectrics via point defect engineering. *Appl Phys Lett* 2025, **126**: 232903.

[8]Li YZ, Zhao JY, Wang Z, *et al.* Ultrahigh Electrostrictive Effect in Lead-Free Sodium Bismuth Titanate-Based Relaxor Ferroelectric Thick Film. *Nanomaterials* 2024, **14**: 1411.

[9] Sun ZX, Xin HY, Diwu LM, et al. Flexible high-temperature piezoelectric nanogenerators for dual-mode energy harvesting and safety monitoring in harsh environments. *Chem Eng J* 2026, **528**: 171919.

[10] Qi H, Chen L, Deng SQ, *et al.* High-entropy ferroelectric materials. *Nat Rev Mater* 2023, **8**: 355–356.

[11] Ge Z, Liu HB, Tang JG, *et al.* Dielectric and electrical energy storage properties of a series of high-entropy tetragonal tungsten bronze ceramics. *J Alloy Compd* 2025, **1015**: 178836.

[12] Yang B, Liu YQ, Lan S, *et al.* High-entropy design for dielectric materials: Status, challenges, and beyond. *J Appl Phys* 2023, **133**: 110904.

[13] Sun ZX, Wang Z, Tian Y, *et al.* Progress, Outlook, and Challenges in Lead-Free Energy-Storage Ferroelectrics. *Adv Electron Mater* 2020, **6**: 1900698.

[14] Ning WZ, Xie JM, Tang LP, *et al.* A high-entropy strategy for enhancing energy storage performance and enabling ultrafast discharge in tungsten bronze ceramics. *J Adv Ceram* 2026, **15**: 9221260.

[15] Peng HN, Wu TT, Liu Z, *et al.* High-entropy relaxor ferroelectric ceramics for ultrahigh energy storage. *Nat Commun* 2024, **15**: 5232.

[16] Sun ZX, Diwu LM, Gao RY, *et al.* Machine Learning-Driven Ultra-High Energy Storage Performance in Ferro-Superparaelectric Capacitors. *Adv Funct Mater* 2026, **36**: e16412.

[17] Liu ZY, Xu SC, Li T, *et al.* Microstructure and ferroelectric properties of high-entropy perovskite oxides with A-site disorder. *Ceram Int* 2021, **47**: 33039–33046.

[18] Zhang M, Xu XZ, Ahmed S, *et al.* Phase transformations in an Aurivillius layer structured ferroelectric designed using the high entropy concept. *Acta Mater* 2022, **229**: 117815.

[19] Zhang CY, Guo WJ, Zhang XC, *et al.* Antiferroelectric to Relaxor Ferroelectric Transition in Na-Doped $K_2PrNb_5O_{15}$ Tetragonal Tungsten Bronzes, *Small* 2025: 2410703.

[20] Sun ZX, Luo TC, Gao P, *et al.* Machine-Learning-Designed BCZT–SBT Heterointerface Unlocks Fatigue-Resistant Energy Storage. *Adv Electron Mater* 2026, **38**: e19635.

[21] Glass AM. Investigation of the Electrical Properties of $Sr_{1-x}Ba_xNb_2O_6$ with Special Reference to Pyroelectric Detection. *J Mater Sci* 1969, **40**: 4699–4713.

[22] Furukawa Y, Makio S, Miyai T, *et al.* Growth and characterization of $K_3Li_2(Ta_xNb_{1-x})_5O_{15}$ crystals for blue second-harmonic-generation applications. *Appl Phys Lett* 1996, **68**: 744–746.

[23] Soejima J, Sato K, Nagata K. Preparation and Characteristics of Ultrasonic Transducers for High Temperature Using $PbNb_2O_6$. *Jpn J Appl Phys* 2000, **39**: 3083.

[24] Krayzman V, Bosak A, Playford HY, *et al.* Incommensurate Modulation and Competing Ferroelectric/Antiferroelectric Modes in Tetragonal Tungsten Bronzes. *Chem Mater* 2022, **34**: 9989–10002.

[25] Levin I, Stennett MC, Miles GC, *et al.* Coupling between octahedral tilting and ferroelectric order in tetragonal tungsten bronze-structured dielectrics. *Appl Phys Lett* 2006, **89**: 122908.

[26]Song JW, Gao Y, Ou YB, *et al.* Role of Incommensurate Modulation in $Ba_4(Sm_{1-x}La_x)_2Ti_4Nb_6O_{30}$ Tetragonal Tungsten Bronzes. *Chem Mater* 2024, **36**: 6720–6730.

[27] Stennett MC, Reaney IM, Miles GC, *et al.* Dielectric and structural studies of $Ba_2MTi_2Nb_3O_{15}$ (BMTNO15, M = Bi^{3+}, La^{3+}, Nd^{3+}, Sm^{3+}, Gd^{3+}) tetragonal tungsten bronze-structured ceramics, *J Appl Phys* 2015, **101**: 104114.

[28] Tidey JP, Dey U, Sanchez AM, *et al.* Structural origins of dielectric anomalies in the filled tetragonal tungsten bronze $Sr_2NaNb_5O_{15}$. *Commun Mater* 2024, **5**: 71.

[29] Murata T, Akamatsu H, Hirai D, *et al.* Antiferroelectricity and robust dielectric response owing to competing polar and antipolar instabilities in tetragonal tungsten bronze K_2 RNb_5O_{15} (*R* : rare-earth). *Phys Rev Materials* 2020, **4**: 104419.

[30] Yang B, Hao SL, Yang P, *et al.* Relaxor behavior and energy storage density induced by B-sites substitutions in $(Ca_{0.28}Ba_{0.72})_{2.1}Na_{0.8}Nb_5O_{15}$ Tungsten bronze ceramics. *Ceram Int* 2018, **44**: 8832–8841.

[31] Peng HN, Liu Z, Fu ZQ, *et al.* Superior Energy Density Achieved in Unfilled Tungsten Bronze Ferroelectrics via Multiscale Regulation Strategy. *Adv Sci* 2023, **10**: 2300227.

[32] Lu CJ, Nie CJ, Duan XF, *et al.* 180° domain structure and its evolution in $Ca_{0.28}Ba_{0.72}Nb_2O_6$ ferroelectric single crystals of tungsten bronzes structure. *Appl Phys Lett* 2006, **88**: 201906.

[33] Wang BW, Koval V, Viola G, *et al.* Investigation of electric field-induced phase transitions in unfilled tungsten bronze relaxor ceramics designed by the high entropy concept. *Acta Mater* 2025, **284**: 120593.

[34] Wang BW, Koval V, Eriksson M, *et al.* High-entropy designed filled tungsten bronze structure ferroelectrics with high Curie temperature and enhanced piezoelectricity. *J Materiomics* 2026, **12**: 101276.

[35] Amira Y, Gagou Y, Menny A, *et al.* Structural and Raman properties of the tetragonal tungsten bronze ferroelectric. *Solid State Commun* 2010, **150**: 419–423.

[36] Xu SD, Shen SJ, Huang CW, *et al.* Enhancing Energy Storage Performance in Lead-Free Bismuth Sodium Niobate-Based Tungsten Bronze Ceramics through Relaxor Tuning. *ACS Appl Mater Interfaces* 2023, **15**: 11642–11651.

[37] Zhu XL, Li K, Chen XM. Ferroelectric Transition and Low-Temperature Dielectric Relaxations in Filled Tungsten Bronzes. *J Am Chem Soc* 2014, **97**: 329–338.

[38] Vugmeister BE, Rabitz H. Dynamics of interacting clusters and dielectric response in relaxor ferroelectrics. *Phys Rev B* 1998, **57**: 7581–7585.

[39] Pirc R, Blinc R. Vogel-Fulcher freezing in relaxor ferroelectrics. *Phys Rev B* 2007, **76**: 020101.

[40] Cao L, Yuan Y, Meng XJ, *et al.* Ferroelectric-Relaxor Crossover and Energy Storage Properties in $Sr_2NaNb_5O_{15}$ -Based Tungsten Bronze Ceramics. *ACS Appl Mater Interfaces* 2022, **14**: 9318–9329.

[41] Burns G, Dacol FH. Glassy polarization behavior in ferroelectric compounds $Pb(Mg_{1/3}Nb_{2/3})O_3$ and $Pb(Zn_{1/3}Nb_{2/3})O_3$. *Solid State Commun* 1983, **48**: 853–856.

[42] Gao YF, Qiao WJ, Lou XJ, *et al.* Ultrahigh Energy Storage in Tungsten Bronze Dielectric Ceramics Through a Weakly Coupled Relaxor Design. *Adv Mate* 2024, **36**: 2310559.

[43] Gardner J, Yu FJ, Tang C, *et al.* Relaxor-to-Ferroelectric Crossover and Disruption of Polar Order in "Empty" Tetragonal Tungsten Bronzes. *Chem Mater* 2016, **28**: 4616–4627.

[44] Bursill LA, Lin PJ. Incommensurate superstructures and phase transition of strontium barium niobate (SBN). *Acta Crystallogr B Struct Sci* 1987, **43**: 49–56.

[45] Gao YF, Song ZZ, Hu HC, *et al.* Optimizing high-temperature energy storage in tungsten bronze-structured ceramics via high-entropy strategy and bandgap engineering. *Nat Commun* 2024, **15**: 2869.